

## RESEARCH ARTICLE

10.1002/2014JA020618

## Key Points:

- Surface absorption causes electron anisotropy and whistler-mode wave growth
- Lunar influence on electrons extends out to 10,000 km or more above the surface
- Lunar magnetic anomalies suppress the electron anisotropy and whistlers

## Correspondence to:

Y. Harada,  
haraday@ssl.berkeley.edu

## Citation:

Harada, Y., J. S. Halekas, A. R. Poppe, S. Kurita, and J. P. McFadden (2014), Extended lunar precursor regions: Electron-wave interaction, *J. Geophys. Res. Space Physics*, 119, doi:10.1002/2014JA020618.

Received 13 SEP 2014

Accepted 5 NOV 2014

Accepted article online 8 NOV 2014

## Extended lunar precursor regions: Electron-wave interaction

Y. Harada<sup>1</sup>, J. S. Halekas<sup>2</sup>, A. R. Poppe<sup>1</sup>, S. Kurita<sup>3</sup>, and J. P. McFadden<sup>1</sup>

<sup>1</sup>Space Sciences Laboratory, University of California, Berkeley, California, USA, <sup>2</sup>Department of Physics and Astronomy, University of Iowa, Iowa City, Iowa, USA, <sup>3</sup>Solar-Terrestrial Environment Laboratory, Nagoya University, Nagoya, Japan

**Abstract** We present Acceleration, Reconnection, Turbulence and Electrodynamics of the Moon's Interaction with the Sun (ARTEMIS) observations of electron-wave interactions which extend to quite large distances upstream from the Moon. We first study electron velocity distributions and wave spectra on an event basis. In both the solar wind and terrestrial plasma sheet, we observe strong whistler wave activity on the magnetic field lines connected to the dayside lunar surface. These whistlers are most likely driven by the anisotropy of upward electrons caused by surface absorption. The whistler growth rates computed from the measured electron distributions successfully reproduced the spectral characteristics of the observed ~100 Hz narrowband oscillations and those reaching lower frequencies. Meanwhile, the incoming solar wind strahl beam is occasionally isotropized near the Moon, and broadband electrostatic waves are observed simultaneously, suggesting streaming instabilities between the incoming and outgoing beams. Based on the case study, we statistically survey the spatial variations of the characteristic quantities of the upstream electron-wave interactions. Both the electron anisotropy and electromagnetic wave intensity decay with increasing field line distances but remain higher than the ambient level at 6 lunar radii (~10,000 km) or more. The strahl electron isotropization and electrostatic waves are found mainly at lower altitudes below 1 lunar radius. The electron anisotropy and whistler intensity exhibit clear anticorrelation with crustal magnetic fields, indicating that the magnetic anomalies suppress the whistler wave growth. The ARTEMIS observations convincingly illustrate that the lunar influence on electrons reaches out to 6 lunar radii or more upstream from the Moon.

## 1. Introduction

The Moon-plasma interaction is characterized by direct exposure of the lunar surface to the ambient plasma owing to the absence of both a significant atmosphere and a global intrinsic magnetic field. Surface absorption of the incoming plasma and rapid diffusion of magnetic fields into the weakly conducting body cause little pressure perturbation in the upstream side, resulting in no bow shock formation even in the supersonic solar wind flow. This leads to a simple picture of the lunar plasma interaction: the upstream plasma hits the Moon without feeling the presence of the Moon and a plasma void is formed behind the Moon.

Recent observations have revealed many aspects of the lunar plasma environment which cannot be represented by this simple description. Approximately 10–20% of the incident protons on the lunar surface are scattered back as neutrals in the solar wind [McComas *et al.*, 2009; Wieser *et al.*, 2009] and in the terrestrial plasma sheet [Harada *et al.*, 2014], whereas fewer protons up to ~1% are backscattered as ions [Saito *et al.*, 2008]. Crustal magnetization of the Moon provides additional particle reflection. Lighter electrons are easily reflected by magnetic mirror force [Anderson *et al.*, 1975; Harada *et al.*, 2013a] and also by electric fields above the negatively charged surface [Halekas *et al.*, 2002; Harada *et al.*, 2012]. Since it is more difficult to deflect heavier ions only by magnetic force, observations of large upward ion fluxes above the magnetic anomalies suggest the presence of electrostatic fields [Saito *et al.*, 2010, 2012; Lue *et al.*, 2011; Futaana *et al.*, 2013]. The backscattered/reflected ions have significant impacts on the plasma environment in the upstream side [Halekas *et al.*, 2013; Fatemi *et al.*, 2014] and in the downstream wake [Nishino *et al.*, 2009, 2010]. In addition, plasma of lunar origin can alter the lunar plasma environment. Pickup ions of lunar exospheric/surface origin [Tanaka *et al.*, 2009; Yokota *et al.*, 2009; Wang *et al.*, 2011; Halekas *et al.*, 2012a; Poppe *et al.*, 2012a] and associated cold electrons possibly modify the ambient plasma and fields in the tail lobes [Harada *et al.*, 2013b; Zhou *et al.*, 2014]. Photoelectrons emitted from the sunlit surface and secondary electrons generated by electron/ion impact are key players determining surface potentials [Halekas *et al.*, 2009; Harada *et al.*, 2013b], which in turn affect the pickup ion dynamics [Poppe *et al.*, 2013] and charged dust grains [Stubbs *et al.*, 2006; Poppe and Horányi, 2010].

In many cases, the perturbed ambient plasma and plasma of lunar origin is unstable enough to drive wave growth. Upstream wave activity is particularly interesting because the detection of plasma perturbation and waves upstream from the Moon means that the ambient plasma can sense the presence of the Moon before it touches the surface. A variety of waves have been observed on the lunar dayside such as <10 Hz electromagnetic waves with many types of spectral characteristics [e.g., Nakagawa *et al.*, 2011; Tsugawa *et al.*, 2011, 2012; Halekas *et al.*, 2013]. These lower frequency waves are often attributed to some ion instabilities. Halekas *et al.* [2012b] reported higher-frequency waves including  $\sim 100$  Hz narrowband electromagnetic waves in the solar wind and terrestrial plasma sheet, and broadband electrostatic waves reaching up to the electron plasma frequency in the plasma sheet. The free energy sources for these higher-frequency electromagnetic and electrostatic waves were associated with the anisotropy of reflected electrons and upward accelerated electron beams, respectively. Such precursor wave activity and deformed electron velocity distributions were also observed at Rhea [Santolik *et al.*, 2011]. The generated waves will eventually smear out the electron loss cones and beams, and no lunar influence will be seen if we go well upstream from the Moon.

This paper presents further analysis on the upstream electron-wave interaction with additional checks on individual events with instability analysis and statistical studies extending the few reported observations by utilizing the large-volume data accumulated by the Acceleration, Reconnection, Turbulence and Electrodynamics of the Moons Interaction with the Sun (ARTEMIS) mission [Angelopoulos, 2011]. We use plasma and field data obtained by ESA (ElectroStatic Analyzer) [McFadden *et al.*, 2008], EFI (Electric Field Instrument) [Bonnell *et al.*, 2008], SCM (Search Coil Magnetometer) [Roux *et al.*, 2008], and FGM (Fluxgate Magnetometer) [Auster *et al.*, 2008] instruments on board ARTEMIS. The highly elliptical orbits of ARTEMIS and huge amount of data accumulated through years of observations by two probes are particularly suited to characterize the spatial variation and evolution of the electron-wave interactions near the Moon. We first show detailed analysis of electron and wave data obtained in the solar wind plasma and terrestrial plasma sheet to describe the characteristics of the electron-wave interactions of interest and to compare them with theoretical predictions. We then present statistical results utilizing characteristic quantities of the phenomena to quantitatively address a fundamental issue concerning the lunar plasma environment: the spatial distributions of the lunar influence on the ambient plasma.

## 2. Case Study

### 2.1. Lunar Dayside Electron Distributions and Wave Activity in the Solar Wind

We first discuss deformed velocity distributions of the solar wind electrons and associated waves on the magnetic field lines connected to the dayside lunar surface. Figure 1 shows an ARTEMIS P2 observation in the solar wind on 8 and 9 May 2013. The magnetic fields are displayed in the selenocentric solar ecliptic (SSE) system (Figure 1j). The SSE system has its  $X$  axis from the Moon toward the Sun, the  $Z$  axis is parallel to the upward normal to the Earth's ecliptic plane, and the  $Y$  completes the orthogonal coordinate set. During this time, the Moon was located at (61, -12, 1) Earth radii in the geocentric solar ecliptic (GSE) coordinate system. The GSE system has its  $X$  axis from the Earth toward the Sun, the  $Z$  axis is parallel to the upward normal to the Earth's ecliptic plane, and the  $Y$  completes the orthogonal coordinate set. As passing over the Moon's dayside, ARTEMIS P2 detected many Moon-related signatures of particles and fields. Among those, Figure 1a shows backscattered protons with energies well below the solar wind beam energy at 00:29–00:48 [Saito *et al.*, 2008; Halekas *et al.*, 2013; Lue *et al.*, 2014] as well as pickup and/or self-pickup ions with higher energies at 23:50–00:12 [Saito *et al.*, 2010; Wang *et al.*, 2011; Halekas *et al.*, 2012a], and Figure 1j exhibits turbulent magnetic fields at 00:31–00:44 possibly related to scattered/reflected ions [Halekas *et al.*, 2006, 2012b; Nakagawa *et al.*, 2011, 2012; Tsugawa *et al.*, 2011, 2012]. In this paper, however, we focus on electron signatures and higher-frequency waves.

We examine electron velocity distributions when the magnetic field line passing through the spacecraft is connected to the dayside lunar surface. Here the magnetic connection is estimated from straight field line tracing from the spacecraft position using 2 s averaged magnetic field data. Figure 1i shows the estimated field line distance to the foot point in units of  $R_L$ , where  $1R_L = 1738$  km. During the unconnected time at 23:30–23:50, 00:25–00:29, 00:44–00:45, 00:48–00:54, and 00:58–01:30 indicated by black in the bottom bar in Figure 1, we observe parallel beams of suprathermal electrons away from the Sun (note that  $B_x < 0$  in the SSE coordinates) and occasional antiparallel beams forming counter-streaming electrons (Figure 1c). The former is a typical signature of the solar wind electron strahl, and the latter is indication of closed field lines

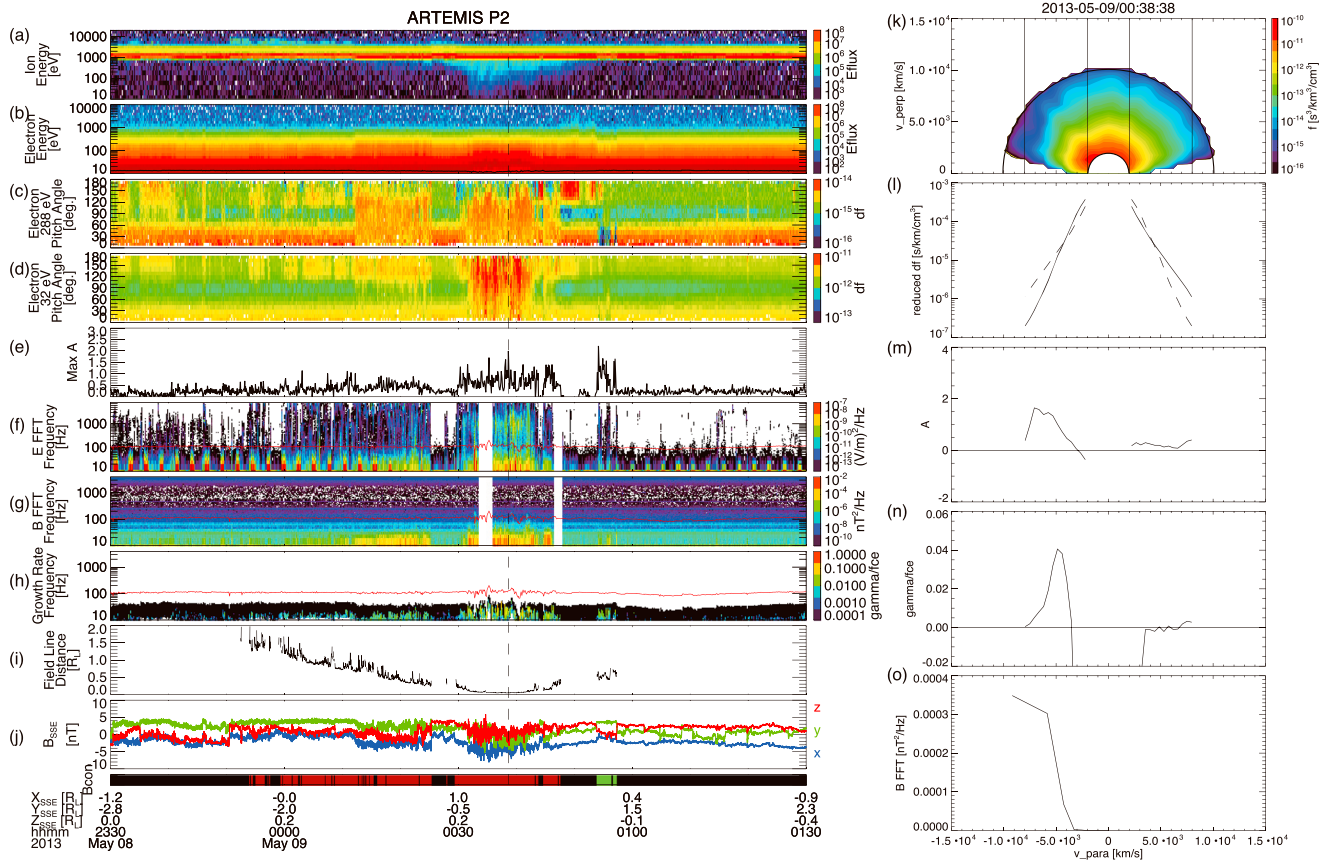


**Figure 1.** Time series data from ARTEMIS P2 in the solar wind on 8 and 9 May 2013. Energy spectra in units of  $eV/cm^2/s/str/eV$  of (a) ions and (b) electrons with the spacecraft potential indicated by the black line, (c) pitch angle spectra in units of  $s^3/km^3/cm^3$  of 288 eV and (d) 32 eV electrons in the plasma rest frame with the spacecraft potential corrected, (e) maximum anisotropy of electrons in the  $2000\text{ km/s} < |v_{||}| < 8000\text{ km/s}$  range, (f) electric and (g) magnetic field wave spectra, (h) growth rates for whistler mode computed from the electron velocity distributions as a function of resonant frequency, (i) distance along the field line to the foot point in units of lunar radii, and (j) 4 Hz magnetic fields in the SSE coordinate system. The bottom color bar shows parallel (red, the magnetic field is toward the Moon) and antiparallel (green, the field is away from the Moon) magnetic connection to the lunar surface. Text labels denote the spacecraft SSE position in units of lunar radii and time of day in UT. The red lines in Figures 1f–h represent the electron cyclotron frequency  $f_{ce}$ . The white regions with no wave spectra in Figures 1f and 1g are due to data gaps. Periodic low-frequency bursts in Figure 1f are due to probe shadowing. Snapshot at 00:38:38 on 8 May 2013 (indicated by the vertical dashed line in the left-hand side panels) of the (k) electron velocity distribution function  $F(v_{||}, v_{\perp})$ , (l) reduced distribution function  $F(v_{||})$ , (m) pitch angle anisotropy  $A(v_{||})$ , (n) whistler growth rate  $\gamma(v_{||})/f_{ce}$ , and (o) magnetic field wave intensity as a function of resonant parallel velocity for whistler-mode waves. The vertical black lines in Figure 1k denote the  $v_{||}$  range ( $2000\text{ km/s} < |v_{||}| < 8000\text{ km/s}$ ) used for computing  $F(v_{||})$ ,  $A(v_{||})$ , and  $\gamma(v_{||})$ . The dashed curves in Figure 1l show  $v_{||}$ -flipped distribution  $F(-v_{||})$ , for reference.

with both ends connected to the Sun [e.g., Gosling et al., 2006]. During the parallel connection interval at 23:50–00:25, 00:29–00:44, and 00:45–00:48 (the magnetic field is toward the Moon, red bars in the bottom), we observe upward (pitch angles  $> 90^\circ$ ) 288 eV electrons from the Moon with near- $180^\circ$  flux bitten out (i.e., loss cone distributions) and 32 eV electrons with upward flux larger than the downward flux. The loss cone distributions are formed by the surface absorption of electrons combined with magnetic reflection by crustal fields [Anderson et al., 1975]. The larger upward flux of lower energy electrons can be explained by energization of electrons as a result of reflection from a moving obstacle in the plasma rest frame [Halekas et al., 2012b]. The energy-dependent loss cones suggest the presence of downward electrostatic fields in addition to crustal magnetic fields above the dayside lunar surface [Halekas et al., 2012c]. We also observe that 288 eV strahl beams are smeared out and become more isotropic at 00:12–00:25, 00:30–00:44, and 00:45–00:48. Previous analysis of Lunar Prospector data showed that the isotropization of incoming electron beams is associated with outgoing electron beams [Halekas et al., 2012c], and we can see that the isotropized strahl electrons (Figure 1c) do coincide with the energized outgoing electrons (Figure 1d). Meanwhile, we see the parallel electron dropouts during the antiparallel connection interval at 00:54–00:57 with a brief unconnected interval at 00:56. These deformed electron velocity distributions are only seen when the

field line is connected to the Moon and the pitch angle spectra return to the ambient distributions once the field line is detached from the Moon.

Figures 1k and 1l show the electron velocity distribution function  $f(v_{\parallel}, v_{\perp})$  and reduced distribution function  $F(v_{\parallel}) = 2\pi \int f(v_{\parallel}, v_{\perp}) v_{\perp} dv_{\perp}$  obtained at 00:38:38 on 9 May 2013 during the parallel connection (indicated by the vertical dashed line in Figures 1a–1j). We can see that the higher-energy part of the  $v_{\parallel} < 0$  electrons are absorbed by the lunar surface (the solid line at  $v_{\parallel} < -5000$  km/s is below the dashed line in Figure 1l) and that the lower energy reflected electrons are energized (the solid line at  $v_{\parallel} > -5000$  km/s is above the dashed line). The incoming  $v_{\parallel} > 0$  electrons become nearly isotropic and no longer form a beam (Figure 1k).

In addition to the modification of solar wind electron velocity distributions, we observe enhanced electrostatic and electromagnetic wave activity during the connected intervals. We see strong broadband electrostatic waves extending up to the highest frequency at 23:54–23:57, 00:00–00:25, 00:29–00:44, 00:45–00:46, and 00:54–00:56 (Figure 1f) and electromagnetic waves below half of the electron cyclotron frequency reaching the lowest frequencies at 00:00–00:25, 00:29–00:44, 00:45–00:46, and 00:54–00:57 (Figures 1f and 1g). The electron cyclotron frequency  $f_{ce}$  is indicated by the red lines in Figures 1f and 1g, and  $f_{ce} \sim 100$  Hz during this time interval. When the field line is temporarily detached from the Moon at 00:25–00:29 and 00:48–00:54, the wave activity ceases immediately, suggesting that these waves are generated under lunar influence. On the other hand, the weaker broadband electrostatic waves during the unconnected interval at 23:30–23:47 may represent wave activity indigenous to the solar wind.

The broadband electrostatic modes observed here resemble those observed in the terrestrial magnetosphere [Halekas et al., 2012b]. The free energy source for the broadband electrostatic waves observed above the dayside lunar surface in the terrestrial magnetosphere was attributed to upward electron beams accelerated through a nonmonotonic surface potential layer [Halekas et al., 2005, 2011; Poppe et al., 2011, 2012b]. As we have seen in Figures 1d and 1l, we have the upward electron beams reflected and accelerated by a moving obstacle. Given the similarity of shapes of the electron distribution functions, instabilities driven by accelerated outgoing beams are plausible mechanisms for the broadband electrostatic wave generation on lunar dayside in the solar wind, though no positive slope is well resolved in Figure 1l. We also note that streaming instabilities between the upward beam electrons and incoming strahl electrons may cause the observed isotropization of strahl beams [Halekas et al., 2012c].

The 10–50 Hz electromagnetic waves were interpreted as whistler-mode waves generated through cyclotron resonance between the upward reflected electrons and downward propagating waves [Halekas et al., 2012b]. Here we conduct additional tests for this explanation using the linear theory [Kennel and Petschek, 1966]. The whistler-mode growth rate  $\gamma$  as a function of resonant velocity  $v_{\parallel}$  and frequency  $f$  is

$$\frac{\gamma(v_{\parallel})}{f_{ce}} = \pi \left(1 - \frac{f}{f_{ce}}\right)^2 \eta(v_{\parallel}) \left[A(v_{\parallel}) - \frac{1}{f_{ce}/f - 1}\right], \quad (1)$$

where the fraction of resonant electrons  $\eta(v_{\parallel})$  is

$$\eta(v_{\parallel}) = v_{\parallel} F(v_{\parallel}) / N_e, \quad (2)$$

the anisotropy  $A(v_{\parallel})$  is

$$A(v_{\parallel}) = \frac{\int \left(v_{\parallel} \frac{\partial f}{\partial v_{\perp}} - v_{\perp} \frac{\partial f}{\partial v_{\parallel}}\right) \frac{v_{\perp}^2}{v_{\parallel}} dv_{\perp}}{2 \int f v_{\perp} dv_{\perp}}, \quad (3)$$

(note that in equation (3)  $f$  stands for the electron distribution function  $f(v_{\parallel}, v_{\perp})$ , not frequency) and the resonant velocity  $v_{\parallel}$  for frequency  $f$  is

$$\frac{v_{\parallel}}{V_{Ae}} = \frac{(1 - f/f_{ce})^{3/2}}{(f/f_{ce})^{1/2}}, \quad (4)$$

where  $V_{Ae} = B / \sqrt{\mu_0 m_e N_e}$  is the electron Alfvén velocity.

Figures 1m and 1n show the anisotropy  $A(v_{\parallel})$  and local growth rate  $\gamma(v_{\parallel})/f_{ce}$  computed from the observed electron distribution function, whereas Figure 1o shows the detected magnetic field wave intensity as a function of resonant parallel velocity  $v_{\parallel}$  for comparison (assuming that the  $v_{\parallel} < 0$  electrons generate

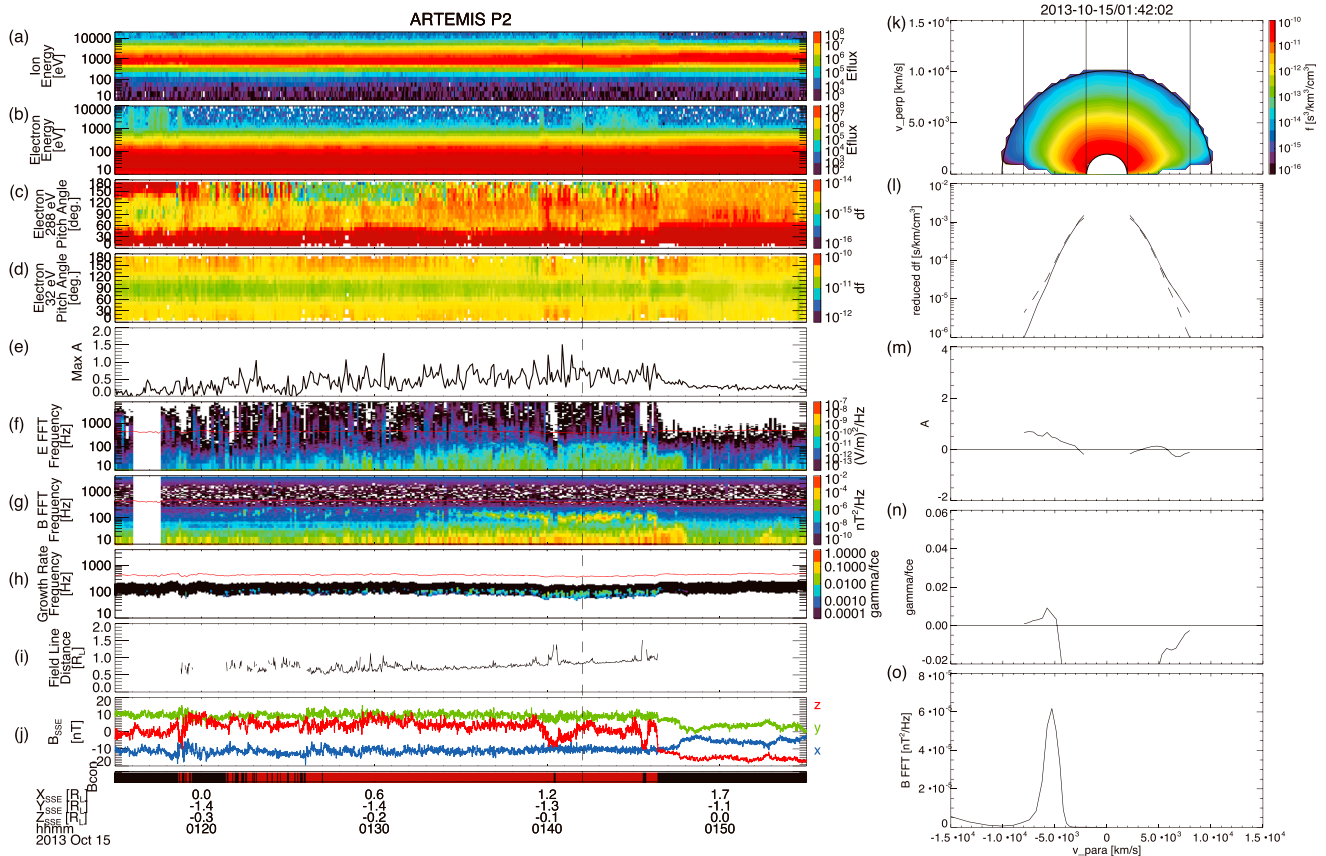


**Figure 2.** Time series and snapshot data from ARTEMIS P2 in the magnetosheath on 15 October 2013 in the same format as Figure 1. The spacecraft potentials during this time interval are below 10 V and not shown in Figure 2b.

waves). We see enhanced wave activity with the unstable  $v_{||}$  range from  $-3500$  to  $-8000$  km/s, suggesting that these waves are generated by the anisotropy associated with the loss cone distribution of reflected electrons. We note that the highest resonant velocity  $v_{||} = -9000$  km/s shown in Figure 1o corresponds to the frequency of 8 Hz, and other free energy sources might contribute to the strong lower frequency wave intensity. Another possibility is that the wave spectrum changed during propagation in an inhomogeneous medium.

Time series of the maximum anisotropy and growth rate as a function of frequency are shown in Figures 1e and 1h. We can see that the maximum anisotropy well represents loss cone distributions seen in the 288 eV electron pitch angle distributions at 00:29–00:44, 00:45–00:48, and 00:54–00:58 (Figure 1c). The computed growth rates are in good agreement with the spectral characteristics of the observed waves (Figures 1g and 1h). The overall agreement between the wave spectra and growth rates derived from the electron distribution functions further confirms that the observed 10–50 Hz electromagnetic waves are driven by the anisotropy of the loss cone distributions of upward electrons.

### 2.2. Narrowband Whistlers

The instability calculation can also explain the narrowband whistlers near half of the electron cyclotron frequency [Halekas et al., 2012b]. Figure 2 shows a narrowband whistler event in the terrestrial magnetosheath in the same format as Figure 1. The Moon was located at  $(-38, 44, 5)$  Earth radii in the GSE system. During the intermittent connected intervals between 01:18 and 01:46, electron loss cones can be identified as flux depletion near  $180^\circ$  in Figure 2c. We observe the distinct narrowband characteristic of  $\sim 100$  Hz electromagnetic waves at 01:21–01:46 (Figures 2f and 2g). The growth rates computed from the measured electron distributions exhibit consistent narrowband nature (Figure 2h).

The narrowband characteristic was explained by the combination of two effects: electrons with larger parallel velocities have smaller fraction of resonant electrons at the lower frequency edge, while smaller parallel

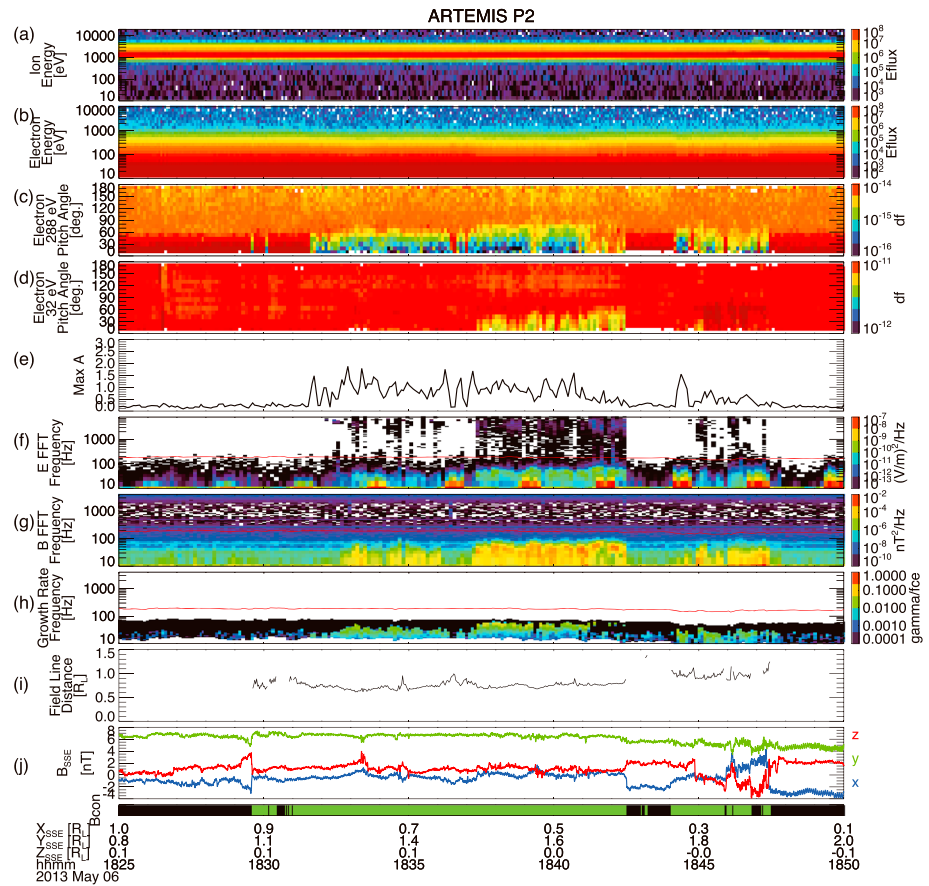


**Figure 3.** Time series data from ARTEMIS P2 in the solar wind on 6 May 2013 in the same format as Figures 1a–1j. The spacecraft potentials during this time interval are below 10 V and not shown in Figure 3b.

velocity electrons have smaller anisotropy to drive wave growth at the higher-frequency edge [Halekas et al., 2012b]. A snapshot of the electron and wave data illustrates that this explanation is plausible (Figures 2k–2o, taken from the time indicated by the vertical dashed line in Figures 2a–2j). At smaller parallel velocities, the anisotropy decreases because of the smaller loss cone population with only small perpendicular velocities and also because of the presence of upward electron beams filling up the loss cone. The smaller anisotropy results in a significant growth rate decrease. On the other hand, there are smaller fraction of resonant electrons  $\eta(v_{\parallel})$  at larger parallel velocities, leading to smaller growth rates in spite of the larger anisotropy. The peaks and distributions of the computed growth rate and observed waves reasonably match within the  $v_{\parallel}$  resolution.

We also find >10 Hz whistler events which exhibit both narrowband nature and extension to lower frequencies. Figure 3 shows one of these events observed when the Moon was in the solar wind at (49, –37, 4) Earth radii in the GSE system. We observe energy-dependent loss cones in upward electrons (pitch angles < 90°) associated with the antiparallel connection at 18:31–18:42 and 18:44–18:47 (Figures 3c and 3d). Narrowband signatures can be identified at 18:41–18:42 in Figure 3g, while broader waves are seen at ~10–80 Hz at 18:32–18:36, 18:37–18:41, and 18:44–18:47 (Figures 3f and 3g). The computed growth rates show intermittent bright spots near 50 Hz at 18:41–18:42 and broader characteristics at 18:32–18:36, 18:37–18:41, and 18:44–18:47 (Figures 3h), which are roughly consistent with the observed wave spectra. Figure 4 shows the estimated foot point locations during this event in comparison with the surface magnetic field strengths. It is seen that the field line foot points are located at weak or moderate crustal field regions and not particularly related to strong magnetic anomalies. This is consistent with the observed large loss cones at higher energies, e.g., those with cutoff pitch angles > 60° at 18:37–18:41 (Figure 3c). The strong whistler emissions observed simultaneously with the large loss cones suggest that these higher-frequency (>10 Hz) whistlers do not result from the solar wind interaction with large and strong magnetic anomalies.

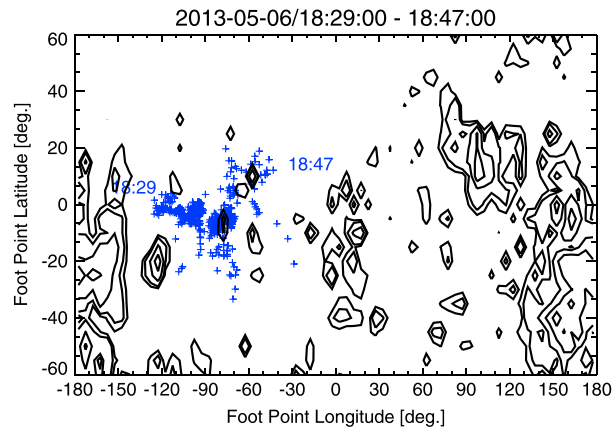


**Figure 4.** Selenographic locations of the estimated field line foot point (blue pluses) during the time interval shown in Figure 3. Surface strength of the crustal magnetic fields derived from Lunar Prospector Magnetometer and Electron Reflectometer measurements is also shown with lines for 10 nT, 20 nT, 50 nT, 100 nT, and 200 nT [Mitchell et al., 2008].

**2.3. Near-Lunar Electron Distributions and Wave Activity in the Terrestrial Plasma Sheet**

Next we show a similar observation in the terrestrial magnetosphere. Figure 5 shows magnetic connection events in the terrestrial plasma sheet with the average lunar GSE position of (−57, 4, 5) Earth radii. During the connected intervals at 19:25, 19:28–19:31, 19:32–19:39, 19:40–19:43, and 19:46–19:49, we observe upward accelerated electron beams at 32 eV (Figure 5c), loss cones at 288 eV (Figure 5d), broadband electrostatic waves reaching up to the electron plasma frequency (Figure 5f), and electromagnetic waves of narrowband nature as well as those extending to lower frequencies (Figure 5f and 5g). The growth rates derived from the electron distributions are in general agreement with the detected wave spectra (Figure 5h).

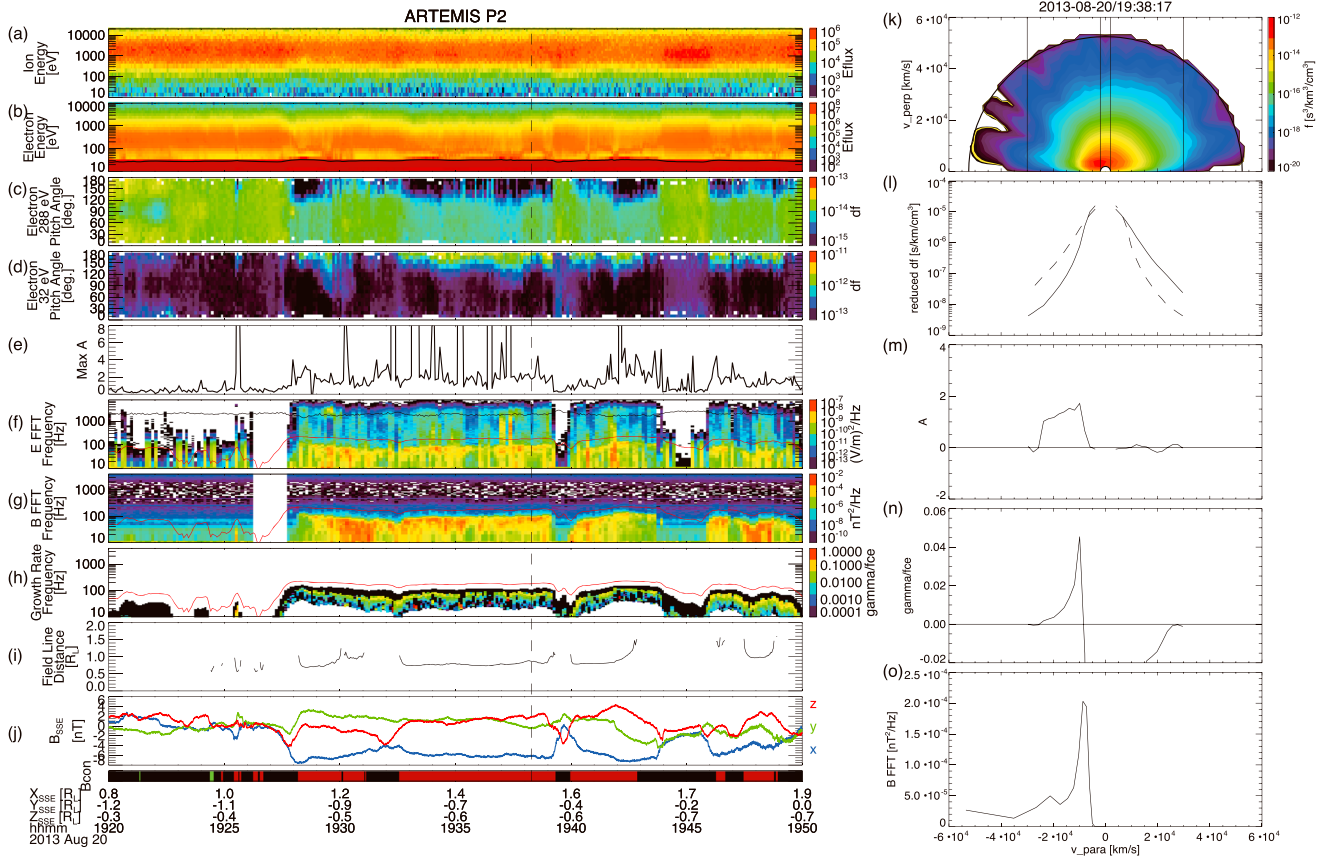


**Figure 5.** Time series and snapshot data from ARTEMIS P2 in the terrestrial plasma sheet on 20 August 2013 in the same format as Figure 1 except that the black line in Figure 5f indicates the electron plasma frequency. The maximum anisotropy,  $F(v_{||})$ ,  $A(v_{||})$ , and  $\gamma(v_{||})$  are now computed in the 2000 km/s <  $|v_{||}|$  < 30,000 km/s range as shown by the vertical lines in Figure 5k, reflecting the higher-electron temperature in the plasma sheet. The spiky bursts of the maximum anisotropy are mostly due to large uncertainty of higher-energy electron flux.

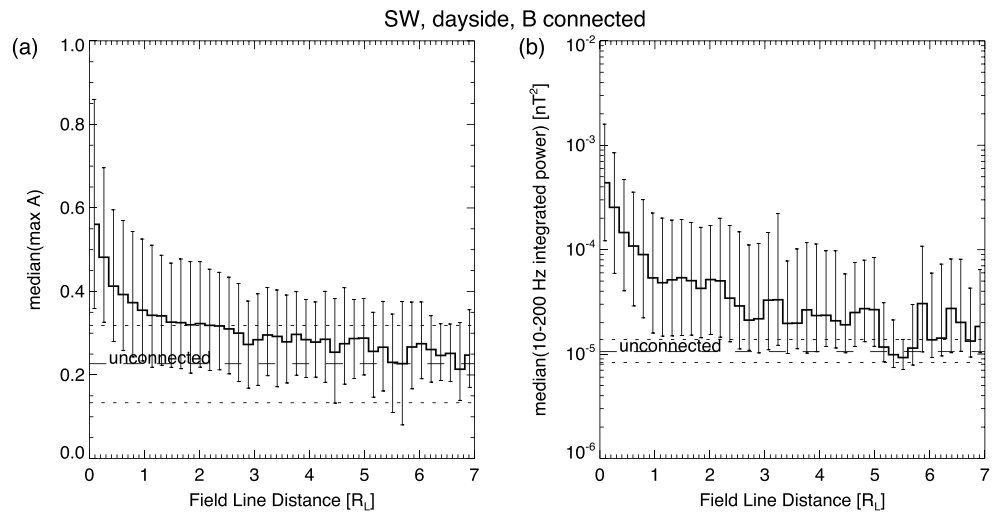


**Figure 6.** Spatial variation of electron loss cones and whistlers along the field line above the Moon's dayside in the solar wind. Medians of (a) maximum anisotropy and (b) magnetic field wave power integrated over 10–200 Hz are shown as a function of field line distance to the foot point. Error bars represent the 25th and 75th percentiles. The dashed and two dotted lines denote the median, 25th, and 75th percentiles during the unconnected intervals for the same condition other than the magnetic connection to the Moon.

A snapshot of the electron distribution function again explains the spectral characteristic of whistlers (Figures 5k–5o at 19:38:17 indicated by the vertical dashed line in Figures 5a–5j). The large anisotropy at parallel velocities of 10,000–25,000 km/s (Figure 5m) and smaller fraction of resonant electrons at larger parallel velocities result in the growth rate distribution that has a sharp peak near the smaller velocity edge with a gradually decaying tail at larger velocities (Figure 5n). The observed wave spectrum has a very similar shape (Figure 5o), validating the explanation of the whistler emission by the anisotropy of upward electrons.

### 3. Statistical Results

We now proceed to characterize statistically the spatial distributions of the electron-wave interactions that we have discussed on a case-by-case basis. We use the maximum anisotropy and magnetic field wave intensity integrated over 10–200 Hz to investigate the loss cone-driven whistlers in both the solar wind and terrestrial plasma sheet. This frequency range corresponds to the whistler-mode band between the lower hybrid frequency  $f_{LHR} \sim 5$  Hz and the electron cyclotron frequency  $f_{ce} \sim 200$  Hz in a typical magnetic field of  $\sim 7$  nT around the Moon. We also investigate the relation between the isotropization of solar wind strahl electrons and electrostatic waves. Using 33 months of measurements from October 2011 to June 2014 by ARTEMIS P1 and P2, the solar wind and plasma sheet intervals are selected as follows. We first divide the data into two groups: the solar wind data ( $-135^\circ < \phi_{MoonGSE} < 135^\circ$ , where  $\phi_{MoonGSE}$  is the azimuthal angle of the lunar position in the GSE coordinates) and tail data (the other). To examine the lunar influence on the upstream solar wind plasma, we restrict the spacecraft position to dayside for the solar wind data:  $-45^\circ < \phi_{scSSE} < 45^\circ$ , where  $\phi_{scSSE}$  is the azimuthal angle of the spacecraft position in the SSE coordinates. We do not separate the solar wind and magnetosheath intervals since the sheath plasma has similar characteristics with the solar wind plasma except that it is shocked. The magnetosheath plasma flow is typically supersonic at lunar orbit, and Moon-plasma interactions similar to those in the solar wind are observed [e.g., Poppe et al., 2014]. Since both the whistler growth rate (according to Figures 1 and 2) and whistler group velocity do not differ much between the magnetosheath and solar wind, we expect that the electron-whistler interaction has similar spatial scales in the two regions. From the tail data, we pick up the usable plasma sheet data based on two conditions: (a) electron temperature  $> 100$  eV to reject the magnetosheath intervals and (b) electron  $\beta > 0.3$  to eliminate the tail lobe data. Here we use the electron  $\beta$  for plasma sheet definition, instead of conventionally used ion  $\beta$  [e.g., Miyashita et al., 2000], to select favorable conditions for the electron-wave growth. We do not have to confine the spacecraft position to the dayside for the plasma sheet data because there is plenty of incident plasma on the lunar nightside in the terrestrial plasma sheet.

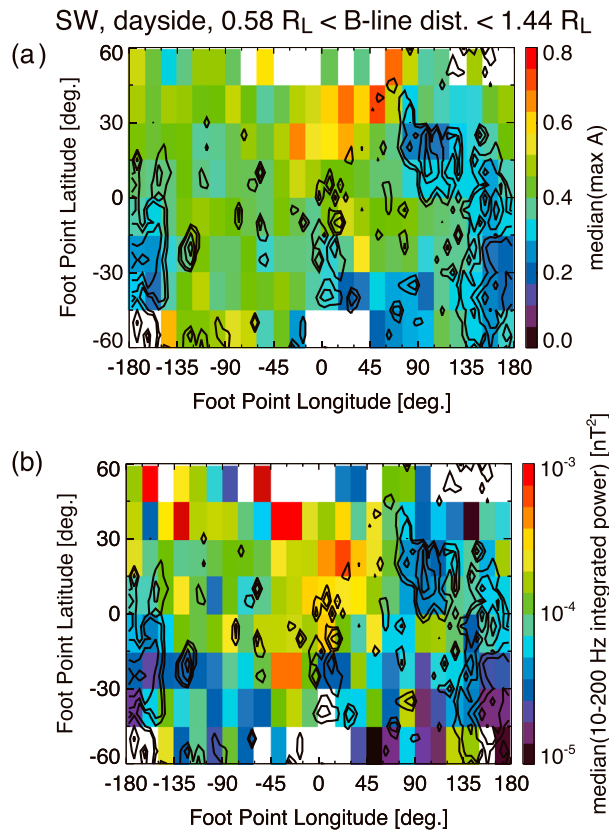


**Figure 7.** Medians of (a) maximum anisotropy and (b) integrated magnetic field wave power for in the solar wind as a function of selenographic locations of the field line foot point, with field line distances between 0.58 and  $1.44R_L$ .

near the Moon  $\gamma \sim 0.01$ ,  $f_{ce} \sim 1$  Hz (from Figures 1 and 2) and a typical whistler group velocity in the solar wind  $V_g \sim$  a few 1000 km/s, we obtain the characteristic  $e$ -folding scale of the linear convective growth  $L = V_g / 2\pi\gamma \sim 100$ s km. This length is several times shorter than, but roughly on the same order of, the characteristic scale length of the sharp decay of the wave amplitude near the Moon  $\sim 1500$  km (according to the  $e$ -folding scale length of the wave power  $\sim 750$  km taken from Figure 6).

We next examine the selenographic dependence of the electron anisotropy and whistler wave intensity since the loss cone angle depends on the magnetic field strength ratio between the spacecraft and surface. Figure 7 shows the electron anisotropy and integrated magnetic field power as a function of the selenographic location of the foot point derived from the data in a fixed field line distance range of  $0.58\text{--}1.44R_L$ . Note that variations of the magnetic field direction, various spacecraft positions relative to the Moon within  $-45^\circ < \phi_{scSSE} < 45^\circ$ , and lunar rotation ( $-135^\circ < \phi_{MoonGSE} < 135^\circ$ ) result in complete coverage of selenographic longitudes with  $15^\circ$  bins. We see that both the anisotropy and wave intensity are clearly anti-correlated with the magnetic anomalies. This result indicates that loss cones on the field lines connected to the strong crustal fields are partially filled up just above the surface, leading to smaller anisotropy and weaker whistler generation at higher altitudes. The weaker wave intensity at stronger crustal fields also suggests that the 10–200 Hz electromagnetic waves have distinctly different sources of free energy from their lower frequency counterparts, because the lower frequency waves tend to be intensified above the magnetic anomalies [Halekas et al., 2006; Tsugawa et al., 2011, 2012; Nakagawa et al., 2012].

### 3.2. Electron Anisotropy and Whistler Waves in the Terrestrial Plasma Sheet

We can pick out similar spatial distributions of the electron anisotropy and whistler wave intensity from the plasma sheet data as well. Figure 8 shows variations of the anisotropy and wave intensity along the connected field line in the terrestrial plasma sheet. The anisotropy distribution exhibits an overall decay with increasing field line distances. The wave intensity is high at distances  $< 1.5R_L$  and drops to lower values at

### 3.1. Electron Anisotropy and Whistler Waves in the Solar Wind

We first present the spatial variation of the anisotropy of electrons and magnetic field wave intensity along the connected field lines to consider how they evolve with altitude. Figure 6 shows the distributions of the maximum anisotropy and integrated electromagnetic wave intensity as a function of the field line distance to the foot point. We can see that both quantities decay sharply at close distances below  $1R_L$  and then decrease gradually as the field line distance increases up to  $\sim 6R_L$ . The anisotropy evolution indicates that the electron loss cones are diffused relatively quickly at low altitudes and gradually at higher altitudes. Note that small but finite shifts of the anisotropy distribution from the unconnected distribution still remain even at  $6R_L$  ( $\sim 10,000$  km) or more above the Moon. Meanwhile, moonward propagating whistlers start to grow at quite large distances  $> 6R_L$  and get enhanced rapidly as the anisotropy increases near the Moon.

We can compare the expected characteristic scale length of the whistler growth with the observed wave intensity distribution. Using a typical growth rate

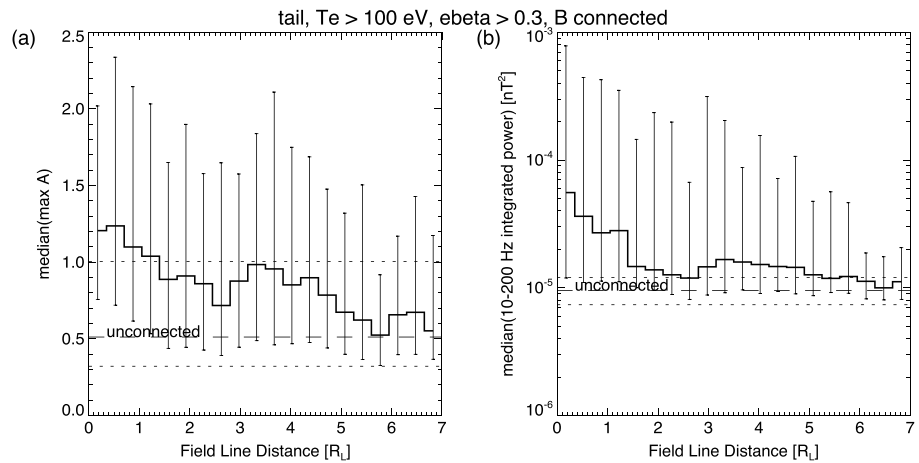


**Figure 8.** Spatial variation of electron anisotropy and whistlers along the field line above the Moon's dayside in the terrestrial plasma sheet in the same format as Figure 6.

larger distances. Both the anisotropy and wave intensity are at higher levels compared to the unconnected intervals even at large distances of  $\sim 6R_L$ . A typical near-lunar growth rate  $\gamma \sim 0.01f_{ce} \sim 1$  Hz (from Figure 5) and a typical whistler group velocity in the plasma sheet  $V_g \sim 10,000$  km/s give  $L \sim 1000$  km. This is roughly

consistent with the sharp decay length of the wave amplitude  $\sim 2500$  km (according to Figure 8). We note that a small bump is seen at  $3\text{--}5R_L$  both in Figures 8a and 8b, but this may simply reflect the data volume insufficient to smooth out event-to-event variations in the plasma sheet.

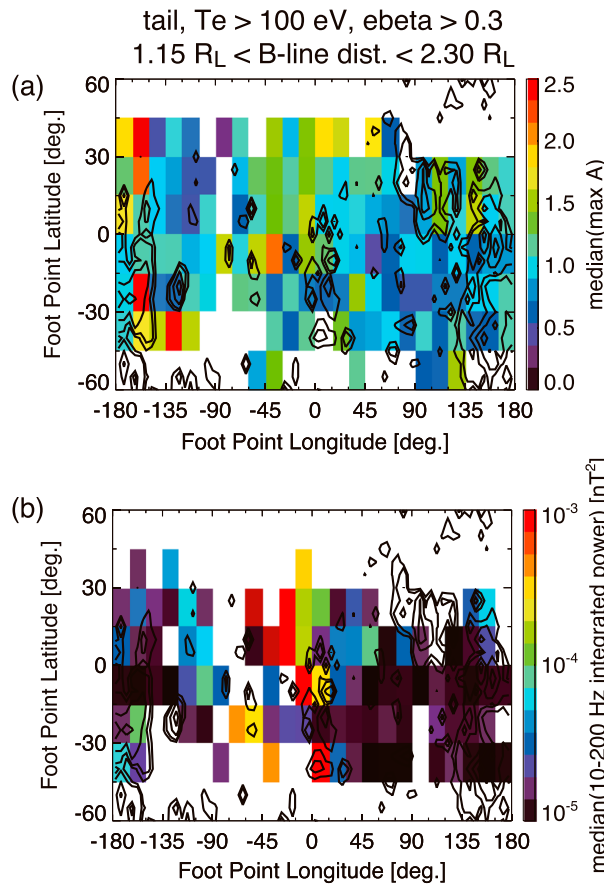


**Figure 9.** Medians of (a) maximum anisotropy and (b) integrated magnetic wave power in the terrestrial plasma sheet as a function of selenographic locations of the field line foot point, with field line distances between  $1.15$  and  $2.30R_L$ .

The selenographic dependence of the anisotropy and wave intensity at a fixed distance range of  $1.15\text{--}2.30R_L$  is shown in Figure 9. The correlation with the crustal field distribution is not as clear as in the solar wind, but we can see a similar trend that the anisotropy and wave intensity decrease with increasing crustal field strength. As we see in the solar wind, the lunar magnetic anomalies tend to suppress higher-frequency whistler growth in the plasma sheet.

### 3.3. Strahl Electron Isotropization and Electrostatic Waves

Here we examine the spatial variations of the isotropization of incoming solar wind electrons and electrostatic wave intensity along the connected field line. Figure 10 shows the ratio of parallel flux (pitch angles of  $0^\circ\text{--}22.5^\circ/157.5^\circ\text{--}180^\circ$ ) over perpendicular flux ( $67.5^\circ\text{--}90^\circ/90^\circ\text{--}112.5^\circ$ ) of incoming  $\sim 285$  eV electrons and the electric field wave intensity

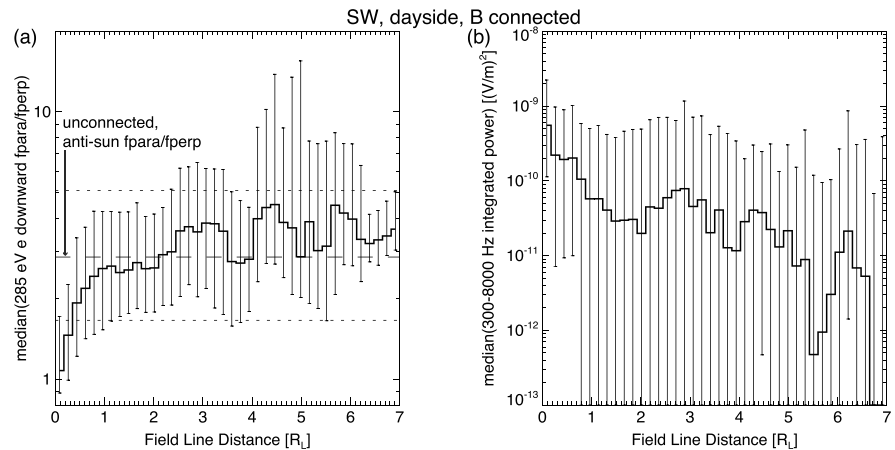


**Figure 10.** Spatial variation of isotropization of incoming strahl electrons and high-frequency electrostatic waves along the field line above the Moon's dayside in the solar wind. Medians of (a) downward parallel/perpendicular flux ratio and (b) electric field wave power integrated over 300–8000 Hz are shown as a function of field line distance to the foot point. Error bars represent the 25th and 75th percentiles. The dashed and two dotted lines in Figure 10a denote the median, 25th, and 75th percentiles of the parallel/perpendicular flux ratio of antisunward electrons during the unconnected intervals. The median, 25th, and 75th percentiles of the integrated electric field power during the unconnected intervals are all below detection level.

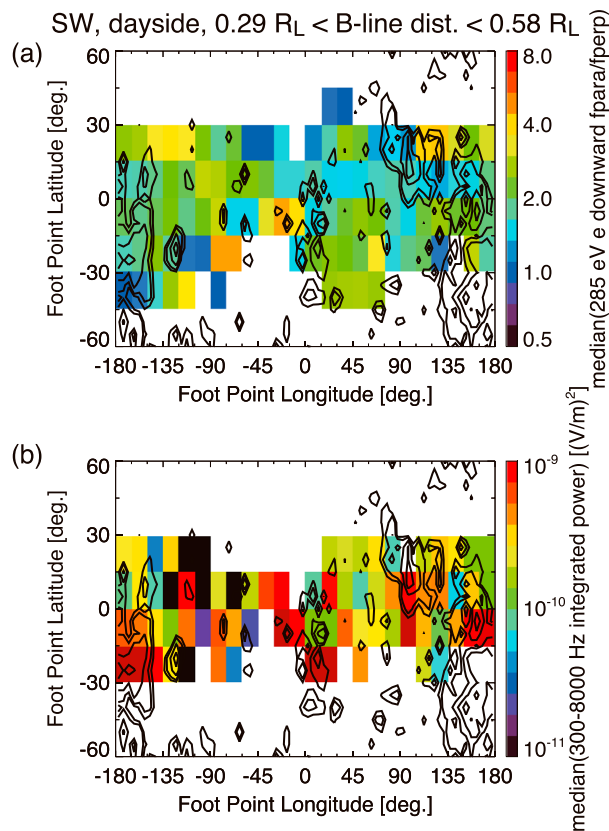


**Figure 11.** Medians of (a) downward parallel/perpendicular flux ratio and (b) integrated electric field wave power in the solar wind as a function of selenographic locations of the field line foot point, with field line distances between 0.29 and 0.58R<sub>L</sub>.

integrated over 300–8000 Hz. This frequency range was chosen to eliminate most of the electric field component of whistlers (the electron cyclotron frequency is typically lower than 300 Hz in the solar wind). We have rejected the electric field wave data if the 10–1000 Hz integrated power exceeds 10<sup>-9</sup> (V/m)<sup>2</sup> to eliminate contamination from the nongeophysical periodic low-frequency bursts (as seen in Figure 1). The flux ratio drops significantly from the unconnected level at small distances < 1R<sub>L</sub>, approaching unity near the Moon (Figure 10a). The significant isotropization region coincides with the strong electrostatic wave region (Figure 10b). This correlation is consistent with the streaming instability scenario that incoming solar wind strahl electrons are isotropized through a streaming instability with outgoing electron beams, generating electrostatic waves. However, the coincidence of electron isotropization and electrostatic waves would not rule out the possibility of pitch angle diffusion by whistlers [Halekas et al., 2012c] because strong whistler waves also coincide with the isotropized electrons (Figure 6b).

Figure 11 shows the selenographic dependence of the strahl isotropization

and electrostatic wave intensity. We see higher levels of electrostatic wave activity over the magnetic anomalies (Figure 11b), suggesting that the broadband electrostatic waves observed in the solar wind are related to magnetically reflected electrons. However, the strahl isotropization (colder colors in Figure 11a) is not particularly associated with the strong crustal field regions. The isotropized flux is found in both anomaly and nonanomaly regions. The apparent lack of selenographic correlations of the strahl isotropization with both electromagnetic and electrostatic waves suggests that neither streaming instabilities nor whistlers are the single cause for scattering the strahl electrons. Both of them and/or other mechanisms might contribute to the isotropization of incoming electron beams.

#### 4. Conclusions

We have analyzed electron velocity distributions and magnetic- and electric-field wave data obtained by ARTEMIS to characterize the electron-wave interactions on the field lines connected to the Moon in the solar wind and terrestrial plasma sheet. Based on the instability analysis, we have confirmed that the anisotropy associated with loss cone distributions drives whistler wave activity including narrowband oscillations near half of the electron cyclotron frequency and those reaching lower frequencies. We also observe broadband electrostatic waves associated with accelerated electron beams upcoming from the Moon in both the solar wind and plasma sheet. In the solar wind, incoming beams of suprathermal electrons are occasionally isotropized at low altitudes.

We have extended our investigation on a statistical basis and quantified the spatial variations of the electron anisotropy and wave activity, utilizing a huge amount of data from 33 month ARTEMIS observations, which are equivalent to 66 month data obtained by two probes. As going upward from the Moon along the connected field line, the electron anisotropy in the solar wind decays sharply at small distances  $< 1R_L$  followed by gradual decrease up to  $6R_L$  or more. The anisotropy in the terrestrial plasma sheet also decays with increasing altitudes and remains higher than the ambient level at  $6R_L$  or more. The magnetic field wave intensity between 10 and 200 Hz exhibits consistent tendencies with the electron anisotropy both in the solar wind and plasma sheet, indicating close connection between the electron loss cone distributions and whistler wave activity. The statistical results have confirmed that the presence of the Moon affects the electrons out to  $6R_L$  or more.

We have also investigated selenographic dependence of the electron anisotropy and 10–200 Hz magnetic field wave activity with data obtained in a certain range of field line distances. Both quantities show clear anticorrelation with the crustal field strength, indicating that the stronger crustal magnetization at the foot point reflects more electrons, leads to smaller initial anisotropy, and results in weaker whistler emissions on that field line. The correlation of electron loss cones and foot point magnetic fields also suggests that electron reflectometry is usable even at large distances over  $0.5R_L$ .

The significant isotropization of incoming solar wind electron beams is observed mainly at close distances  $< 1R_L$  from the Moon's dayside. Its coincidence with strong electrostatic waves suggests streaming instabilities between the inward beam electrons and outward reflected beam/conic electrons. Since the isotropization also coincides with the strong whistler emissions, another possible scenario is that whistler waves generated by the electron anisotropy cause the pitch angle diffusion of incoming beam electrons. The apparent lack of selenographic correlations of the isotropization with electrostatic and electromagnetic wave intensities as well as with magnetic anomalies suggests that both scenarios and/or other processes are responsible for modifying the incoming electron distributions.

Our observations have shown that the lunar precursor region extends to great distances from the Moon. The surface absorption and magnetic reflection of incident electrons give rise to highly anisotropic upward electrons, which drive whistler-mode wave growth as far as  $\sim 6R_L$  above the Moon. The strong magnetic reflection suppresses the loss cone-driven whistlers unlike many other waves that are enhanced above crustal magnetic anomalies. In addition, incoming electron beams are sometimes modified near the Moon possibly as a result of streaming instabilities with outgoing accelerated electrons and/or pitch angle scattering by pregenerated whistlers. The upstream Moon-electron interaction region studied in this paper is just one aspect of the whole Moon-plasma interaction region. Further studies will be required to fully characterize the lunar plasma environment which hosts a variety of fascinating plasma phenomena.

### Acknowledgments

We acknowledge NASA contract NASS-02099 and V. Angelopoulos for the use of data from the THEMIS Mission, J.W. Bonnell and F.S. Mozer for the use of EFI data, A. Roux and O. LeContel for the use of SCM data, and K.H. Glassmeier, U. Auster, and W. Baumjohann for the use of FGM data provided under the lead of the Technical University of Braunschweig and with financial support through the German Ministry for the Economy and Technology and the German Center for Aviation and Space (DLR) under contract 50 OC 0302. We gratefully acknowledge support from NASA's Solar System Exploration Research Virtual Institute (SSERVI), grant #NNX14AG16A. ARTEMIS data are publicly available at <http://artemis.ssl.berkeley.edu>.

Yuming Wang thanks the reviewers for their assistance in evaluating this paper.

### References

- Anderson, K. A., R. P. Lin, R. E. McGuire, and J. E. McCoy (1975), Measurement of lunar and planetary magnetic fields by reflection of low energy electrons, *Space Sci. Instrum.*, *1*, 439–470.
- Angelopoulos, V. (2011), The ARTEMIS mission, *Space Sci. Rev.*, *165*(1–4), 3–25, doi:10.1007/s11214-010-9687-2.
- Auster, H. U., et al. (2008), The THEMIS fluxgate magnetometer, *Space Sci. Rev.*, *141*(1–4), 235–264, doi:10.1007/s11214-008-9365-9.
- Bonnell, J. W., F. S. Mozer, G. T. Delory, A. J. Hull, R. E. Ergun, C. M. Cully, V. Angelopoulos, and P. R. Harvey (2008), The electric field instrument (EFI) for THEMIS, *Space Sci. Rev.*, *141*(1–4), 303–341, doi:10.1007/s11214-008-9469-2.
- Fatemi, S., M. Holmström, Y. Futaana, C. Lue, M. R. Collier, S. Barabash, and G. Stenberg (2014), Effects of protons reflected by lunar crustal magnetic fields on the global lunar plasma environment, *J. Geophys. Res. Space Physics*, *119*, 6095–6105, doi:10.1002/2014JA019900.
- Futaana, Y., S. Barabash, M. Wieser, C. Lue, P. Wurz, A. Vorburger, A. Bhardwaj, and K. Asamura (2013), Remote energetic neutral atom imaging of electric potential over a lunar magnetic anomaly, *Geophys. Res. Lett.*, *40*, 262–266, doi:10.1002/grl.50135.
- Gosling, J., D. McComas, R. Skoug, and C. Smith (2006), Magnetic reconnection at the heliospheric current sheet and the formation of closed magnetic field lines in the solar wind, *Geophys. Res. Lett.*, *33*, L17102, doi:10.1029/2006GL027188.
- Halekas, J. S., D. L. Mitchell, R. P. Lin, L. L. Hood, M. H. Acuña, and A. B. Binder (2002), Evidence for negative charging of the lunar surface in shadow, *Geophys. Res. Lett.*, *29*(10), 1435, doi:10.1029/2001GL014428.
- Halekas, J. S., R. P. Lin, and D. L. Mitchell (2005), Large negative lunar surface potentials in sunlight and shadow, *Geophys. Res. Lett.*, *32*, L09102, doi:10.1029/2005GL022627.
- Halekas, J. S., D. A. Brain, D. L. Mitchell, and R. P. Lin (2006), Whistler waves observed near lunar crustal magnetic sources, *Geophys. Res. Lett.*, *33*, L22104, doi:10.1029/2006GL027684.
- Halekas, J. S., G. T. Delory, R. P. Lin, T. J. Stubbs, and W. M. Farrell (2009), Lunar prospector measurements of secondary electron emission from lunar regolith, *Planet. Space Sci.*, *57*, 78–82, doi:10.1016/j.pss.2008.11.009.
- Halekas, J. S., G. T. Delory, W. M. Farrell, V. Angelopoulos, J. P. McFadden, J. W. Bonnell, M. O. Fillingim, and F. Plaschke (2011), First remote measurements of lunar surface charging from ARTEMIS: Evidence for nonmonotonic sheath potentials above the dayside surface, *J. Geophys. Res.*, *116*, A07103, doi:10.1029/2011JA016542.
- Halekas, J. S., A. R. Poppe, G. T. Delory, M. Sarantos, W. M. Farrell, V. Angelopoulos, and J. P. McFadden (2012a), Lunar pickup ions observed by ARTEMIS: Spatial and temporal distribution and constraints on species and source locations, *J. Geophys. Res.*, *117*, E06006, doi:10.1029/2012JE004107.
- Halekas, J. S., et al. (2012b), Lunar precursor effects in the solar wind and terrestrial magnetosphere, *J. Geophys. Res.*, *117*, A05101, doi:10.1029/2011JA017289.
- Halekas, J. S., A. Poppe, G. T. Delory, W. M. Farrell, and M. Horányi (2012c), Solar wind electron interaction with the dayside lunar surface and crustal magnetic fields: Evidence for precursor effects, *Earth Planets Space*, *64*, 73–82.
- Halekas, J. S., A. R. Poppe, J. P. McFadden, and K.-H. Glassmeier (2013), The effects of reflected protons on the plasma environment of the Moon for parallel interplanetary magnetic fields, *Geophys. Res. Lett.*, *40*, 4544–4548, doi:10.1002/grl.50892.
- Harada, Y., et al. (2012), Nongyrotropic electron velocity distribution functions near the lunar surface, *J. Geophys. Res.*, *117*, A07220, doi:10.1029/2012JA017642.
- Harada, Y., et al. (2013a), Small-scale magnetic fields on the lunar surface inferred from plasma sheet electrons, *Geophys. Res. Lett.*, *40*, 3362–3366, doi:10.1002/grl.50662.
- Harada, Y., S. Machida, J. S. Halekas, A. R. Poppe, and J. P. McFadden (2013b), ARTEMIS observations of lunar dayside plasma in the terrestrial magnetotail lobe, *J. Geophys. Res. Space Physics*, *118*, 3042–3054, doi:10.1002/jgra.50296.
- Harada, Y., et al. (2014), Backscattered energetic neutral atoms from the Moon in the Earth's plasma sheet observed by Chandrayaan-1/sub-kev atom reflecting analyzer instrument, *J. Geophys. Res. Space Physics*, *119*(5), 3573–3584, doi:10.1002/2013JA019682.
- Kennel, C. F., and H. E. Petschek (1966), Limit on stably trapped particle fluxes, *J. Geophys. Res.*, *71*, 1–28, doi:10.1029/JZ071i001p00001.
- Lue, C., Y. Futaana, S. Barabash, M. Wieser, M. Holmström, A. Bhardwaj, M. B. Dhanya, and P. Wurz (2011), Strong influence of lunar crustal fields on the solar wind flow, *Geophys. Res. Lett.*, *38*, L03202, doi:10.1029/2010GL046215.
- Lue, C., Y. Futaana, S. Barabash, M. Wieser, A. Bhardwaj, and P. Wurz (2014), Chandrayaan-1 observations of backscattered solar wind protons from the lunar regolith: Dependence on the solar wind speed, *J. Geophys. Res. Planets*, *119*, 968–975, doi:10.1002/2013JE004582.
- McComas, D. J., et al. (2009), Lunar backscatter and neutralization of the solar wind: First observations of neutral atoms from the Moon, *Geophys. Res. Lett.*, *36*, L12104, doi:10.1029/2009GL038794.
- McFadden, J. P., C. W. Carlson, D. Larson, M. Ludlam, R. Abiad, B. Elliott, P. Turin, M. Marckwardt, and V. Angelopoulos (2008), The THEMIS ESA plasma instrument and in-flight calibration, *Space Sci. Rev.*, *141*(1–4), 277–302, doi:10.1007/s11214-008-9440-2.
- Mitchell, D. L., J. S. Halekas, R. P. Lin, S. Frey, L. L. Hood, M. H. Acuña, and A. Binder (2008), Global mapping of lunar crustal magnetic fields by Lunar Prospector, *Icarus*, *194*, 401–409, doi:10.1016/j.icarus.2007.10.027.
- Miyashita, Y., S. Machida, T. Mukai, Y. Saito, K. Tsuruda, H. Hayakawa, and P. R. Sutcliffe (2000), A statistical study of variations in the near and mid-tail magnetotail associated with substorm onsets: Geotail observations, *J. Geophys. Res.*, *105*(A7), 15,913–15,930, doi:10.1029/1999JA000392.
- Nakagawa, T., F. Takahashi, H. Tsunakawa, H. Shibuya, H. Shimizu, and M. Matsushima (2011), Non-monochromatic whistler waves detected by Kaguya on the dayside surface of the Moon, *Earth Planets Space*, *63*(1), 37–46, doi:10.5047/eps.2010.01.005.
- Nakagawa, T., A. Nakayama, F. Takahashi, H. Tsunakawa, H. Shibuya, H. Shimizu, and M. Matsushima (2012), Large-amplitude monochromatic ULF waves detected by Kaguya at the Moon, *J. Geophys. Res.*, *117*, A04101, doi:10.1029/2011JA017249.
- Nishino, M. N., et al. (2009), Solar-wind proton access deep into the near-Moon wake, *Geophys. Res. Lett.*, *36*, L16103, doi:10.1029/2009GL039444.
- Nishino, M. N., et al. (2010), Effect of the solar wind proton entry into the deepest lunar wake, *Geophys. Res. Lett.*, *37*, L12106, doi:10.1029/2010GL043948.
- Poppe, A., and M. Horányi (2010), Simulations of the photoelectron sheath and dust levitation on the lunar surface, *J. Geophys. Res.*, *115*, A08106, doi:10.1029/2010JA015286.
- Poppe, A., J. S. Halekas, and M. Horányi (2011), Negative potentials above the day-side lunar surface in the terrestrial plasma sheet: Evidence of non-monotonic potentials, *Geophys. Res. Lett.*, *38*, L02103, doi:10.1029/2010GL046119.
- Poppe, A. R., R. Samad, J. S. Halekas, M. Sarantos, G. T. Delory, W. M. Farrell, V. Angelopoulos, and J. P. McFadden (2012a), ARTEMIS observations of lunar pick-up ions in the terrestrial magnetotail lobes, *Geophys. Res. Lett.*, *39*, L17104, doi:10.1029/2012GL052909.
- Poppe, A. R., J. S. Halekas, G. T. Delory, W. M. Farrell, V. Angelopoulos, J. P. McFadden, J. W. Bonnell, and R. E. Ergun (2012b), A comparison of ARTEMIS observations and particle-in-cell modeling of the lunar photoelectron sheath in the terrestrial magnetotail, *Geophys. Res. Lett.*, *39*, L01102, doi:10.1029/2011GL050321.

- Poppe, A. R., J. S. Halekas, R. Samad, M. Sarantos, and G. T. Delory (2013), Model-based constraints on the lunar exosphere derived from ARTEMIS pickup ion observations in the terrestrial magnetotail, *J. Geophys. Res. Planets*, *118*, 1135–1147, doi:10.1002/jgre.20090.
- Poppe, A. R., S. Fatemi, J. S. Halekas, M. Holmström, and G. T. Delory (2014), ARTEMIS observations of extreme diamagnetic fields in the lunar wake, *Geophys. Res. Lett.*, *41*, 3766–3773, doi:10.1002/2014GL060280.
- Roux, A., O. Le Contel, C. Coillot, A. Bouabdellah, B. de la Porte, D. Alison, S. Ruocco, and M. C. Vassal (2008), The search coil magnetometer for THEMIS, *Space Sci. Rev.*, *141*(1–4), 265–275, doi:10.1007/s11214-008-9455-8.
- Saito, Y., et al. (2008), Solar wind proton reflection at the lunar surface: Low energy ion measurement by MAP-PACE onboard SELENE (KAGUYA), *Geophys. Res. Lett.*, *35*, L24205, doi:10.1029/2008GL036077.
- Saito, Y., et al. (2010), In-Flight performance and initial results of plasma energy angle and composition experiment (PACE) on SELENE (Kaguya), *Space Sci. Rev.*, *154*, 265–303, doi:10.1007/s11214-010-9647-x.
- Saito, Y., M. N. Nishino, M. Fujimoto, T. Yamamoto, S. Yokota, H. Tsunakawa, H. Shibuya, M. Matsushima, H. Shimizu, and F. Takahashi (2012), Simultaneous observation of the electron acceleration and ion deceleration over lunar magnetic anomalies, *Earth Planets Space*, *64*, 83–92.
- Santolík, O., D. A. Gurnett, G. H. Jones, P. Schippers, F. J. Cray, J. S. Leisner, G. B. Hospodarsky, W. S. Kurth, C. T. Russell, and M. K. Dougherty (2011), Intense plasma wave emissions associated with Saturn's Moon Rhea, *Geophys. Res. Lett.*, *38*, L19204, doi:10.1029/2011GL049219.
- Stubbs, T., R. Vondrak, and W. Farrell (2006), A dynamic fountain model for lunar dust, *Adv. Space Res.*, *37*(1), 59–66, doi:10.1016/j.asr.2005.04.048.
- Tanaka, T., et al. (2009), First in situ observation of the Moon-originating ions in the Earth's magnetosphere by MAP-PACE on SELENE (KAGUYA), *Geophys. Res. Lett.*, *36*, L22106, doi:10.1029/2009GL040682.
- Tsugawa, Y., N. Terada, Y. Katoh, T. Ono, H. Tsunakawa, F. Takahashi, H. Shibuya, H. Shimizu, and M. Matsushima (2011), Statistical analysis of monochromatic whistler waves near the Moon detected by Kaguya, *Ann. Geophys.*, *29*(5), 889–893, doi:10.5194/angeo-29-889-2011.
- Tsugawa, Y., et al. (2012), Statistical study of broadband whistler-mode waves detected by Kaguya near the Moon, *Geophys. Res. Lett.*, *39*, L16101, doi:10.1029/2012GL052818.
- Wang, X. D., et al. (2011), Detection of  $m/q = 2$  pickup ions in the plasma environment of the Moon: The trace of exospheric  $H_2^+$ , *Geophys. Res. Lett.*, *38*, L14204, doi:10.1029/2011GL047488.
- Wieser, M., et al. (2009), Extremely high reflection of solar wind protons as neutral hydrogen atoms from regolith in space, *Planet. Space Sci.*, *57*(14–15), 2132–2134, doi:10.1016/j.pss.2009.09.012.
- Yokota, S., et al. (2009), First direct detection of ions originating from the Moon by MAP-PACE IMA onboard SELENE (KAGUYA), *Geophys. Res. Lett.*, *36*, L11201, doi:10.1029/2009GL038185.
- Zhou, X. Z., V. Angelopoulos, A. R. Poppe, J. S. Halekas, K. K. Khurana, M. G. Kivelson, S. Fatemi, and M. Holmström (2014), Lunar dayside current in the terrestrial lobe: ARTEMIS observations, *J. Geophys. Res. Space Physics*, *119*, 3381–3391, doi:10.1002/2014JA019842.